INTERNATIONAL JOURNAL FOR NUMERICAL METHODS IN FLUIDS
Int. J. Numer. Meth. Fluids 2006; **52**:297–319
Published online 10 February 2006 in Wiley InterScience (www.interscience.wiley.com). DOI: 10.1002/fld.1180

A finite volume method for viscous incompressible flows using a consistent flux reconstruction scheme

A. Roy[1,‡] and G. Bandyopadhyay[2,*,†]

[1]*Department of Space Engineering and Rocketry, Birla Institute of Technology, Mesra, Ranchi 835 215, India*
[2]*Department of Aerospace Engineering, Indian Institute of Technology, Kharagpur 721 302, India*

SUMMARY

An incompressible Navier–Stokes solver using curvilinear body-fitted collocated grid has been developed to solve unconfined flow past arbitrary two-dimensional body geometries. In this solver, the full Navier–Stokes equations have been solved numerically in the physical plane itself without using any transformation to the computational plane. For the proper coupling of pressure and velocity field on collocated grid, a new scheme, designated 'consistent flux reconstruction' (CFR) scheme, has been developed. In this scheme, the cell face centre velocities are obtained explicitly by solving the momentum equations at the centre of the cell faces. The velocities at the cell centres are also updated explicitly by solving the momentum equations at the cell centres. By resorting to such a fully explicit treatment considerable simplification has been achieved compared to earlier approaches. In the present investigation the solver has been applied to unconfined flow past a square cylinder at zero and non-zero incidence at low and moderate Reynolds numbers and reasonably good agreement has been obtained with results available from literature. Copyright © 2006 John Wiley & Sons, Ltd.

KEY WORDS: curvilinear collocated grid; incompressible Navier–Stokes solver; finite volume method; physical plane; explicit–explicit scheme; consistent flux reconstruction

1. INTRODUCTION

Staggered grid was widely used in the early Navier–Stokes solvers, particularly for solving flow problems on a Cartesian coordinate system [1–3]. Use of staggered grid provides a strong pressure–velocity coupling that is automatically achieved by virtue of the location of the various variables in the cell and thereby avoids the occurrence of odd–even pressure oscillations that often occur in collocated grid arrangements. However, in the recent times numerous researchers have introduced explicit or implicit artificial diffusion in collocated grid-based schemes for effective coupling of the governing equations and achieved satisfactory solution. Sotiropoulos and Abdallah [4] report the development of a coupled fully implicit scheme

*Correspondence to: G. Bandyopadhyay, Department of Aerospace Engineering, Indian Institute of Technology, Kharagpur 721 302, India.
†E-mail: gbandyo@aero.iitkgp.ernet.in
‡E-mail: roy_arnab2001@yahoo.com, roy_arnab2005@rediffmail.com

Received 5 May 2005
Revised 14 September 2005
Accepted 20 November 2005

for solving steady incompressible Navier–Stokes equations on a collocated grid in which the momentum equations are coupled with a pressure Poisson equation. No explicit artificial diffusion has been used in the scheme, but the pressure equation introduces dissipative terms that are second-order spatial derivatives of pressure into the governing equations. Fourth-order artificial diffusion terms need to be incorporated to eliminate the odd–even spurious pressure oscillations on a collocated grid when the governing equations are solved in a coupled manner [5]. de Foy and Dawes [6] have developed a finite volume incompressible flow solver for three-dimensional unsteady flows based on an unstructured tetrahedral mesh with collocation of the flow variables at the cell vertices. The authors use artificial dissipation in solving the momentum equations and pressure correction step to prevent the formation of instabilities. Kim and Moin [7] point out that instabilities, which occur especially at high Reynolds numbers can be handled and a stable solution can be produced by explicit or implicit introduction of artificial diffusion.

In spite of the strong pressure–velocity coupling available on staggered grid, it is problematic for calculating flow problems on general curvilinear coordinate system since the solution process is not carried out in the physical plane but in the transformed plane. In such an approach, where both independent and dependent variables are transformed from the Cartesian form of the equations, the curvature of the coordinate lines occurs through the so-called Christoffel symbols in the momentum equations. This results in a source term that blends the physics of the flow with the geometry of the grid and makes the momentum equations non-conservative [8, 9]. Moreover, the transformed equations are very complex, because of the associated contravariant and covariant velocity components and accurate calculation of the higher-order derivatives involved in the Christoffel symbols is difficult. Also, such systems suffer from uncontrolled intrinsic numerical diffusion in a decoupled approach.

To circumvent this problem, attempts have been made in the last two decades to develop Navier–Stokes solvers for incompressible flow calculations using collocated grid in curvilinear coordinate systems. In this approach the Cartesian velocity components are retained in the Navier–Stokes equations and the problem is solved in the physical plane. However, in collocated grid the mass fluxes involved in the integral form of the continuity equation are not available as dependent variables, and consequently, they must be interpolated. This interpolation should be carried out by a suitable flux reconstruction scheme. If the flow variables at the cell faces are approximated by a simple linear interpolation of adjoining nodal values, problem arises from the development of spurious pressure modes and odd–even decoupling. In order to ensure a strong coupling between the velocity and pressure fields, a better (i.e. physically consistent interpolation) scheme needs to be used.

A major breakthrough in this respect has been made by Rhie and Chow [10] in their physical interpolation approach (PIA). A flux reconstruction expression at the cell face that replicates a momentum equation was developed by them. In their approach, the pressure gradient is discretized at the cell face while the remaining terms in the momentum equations are interpolated. This flux reconstruction approach uses a 9-point stencil for the pressure terms and 21-point stencil for the cell face velocity calculations. The resulting reconstructed flux is used only in the continuity equation to prevent the occurrence of spurious pressure modes. The reconstructed flux has not been used in the momentum equations. To ensure stability, the hybrid scheme is used to discretize the momentum equations. Matrix inversion has been used at both the steps, i.e. for cell face flux reconstruction and solution of momentum equations, and thereby makes the scheme (implicit–implicit) somewhat complex. However, most authors

working with the collocated grid arrangements have used this method of pressure–velocity coupling during the last two decades.

Schneider and Raw [11] deduced the flux reconstruction formulae for the cell face variables from the discretized form of the momentum equations and these were used in the continuity as well as the momentum equations to update the flow variables. A control volume node-centred finite element method has been used in this method. Matrix inversion has been used for solving both the steps, making this an implicit–implicit scheme. However, this PIA has an advantage of using a compact 9-point stencil for both pressure and cell face velocity calculations. The method suffers from some accuracy problem for the diffusive terms as pointed out by Deng *et al.* [12].

Utilizing the idea of Schneider and Raw [11], Deng *et al.* [12] devised a consistent physical interpolation (CPI) approach by considering a compact 9-point stencil closure for the pressure as well as the cell face velocities. This approach determines the cell face variables by an explicit manner, thereby circumventing the problem of matrix inversion of Rhie and Chow [10] and Schneider and Raw [11] for solving the cell face velocities and also overcomes the accuracy problem of Schneider and Raw [11] scheme. However, Deng *et al.* [12] used the explicit scheme only to calculate the cell face velocities whereas the flow variables at the cell centres were updated by using an implicit scheme (explicit–implicit scheme).

Considerable benefits can be achieved by developing a method in which calculation of both cell face velocities and the flow variables at the cell centres are carried out in a fully explicit (explicit–explicit) manner. An attempt to develop such a fully explicit method is presented here.

In the present solver, a fully explicit scheme is adopted for the calculation of both cell face velocities and the flow variables at the cell centres. For the calculation of cell face velocities a 'consistent flux reconstruction' (CFR) technique has been formulated which is based on solving the momentum equations at each cell face explicitly. The flux reconstruction cell on a face of the control volume is placed centrally between the two cells that share that face. If the grid gets stretched near a sharp corner, there is provision in the grid generation code to cluster and smooth the grid in that location such that the discretization error in the flux reconstruction step is minimized. Two pressure nodes are located at two opposite faces of the flux reconstruction cell. A 9-point stencil is used for the pressure equation and a 13-point stencil for the velocity calculations. A discrete pressure Poisson equation is obtained by substituting the reconstructed cell face velocities in the discrete continuity equation. The pressure Poisson equation is solved iteratively using successive over-relaxation scheme. The reconstructed cell face flux is substituted in both the continuity and momentum equations. For updating the flow variables at the cell centres, the momentum equations are solved in an explicit manner in contrast to the implicit scheme of Deng *et al.* [12].

The present solver, developed on the basis of CFR scheme, is capable of calculating unconfined flow past any arbitrary two-dimensional body geometry. In the present investigation, unconfined flow past a square cylinder has been computed over a range of Reynolds number for angles of incidence varying from 0 to 45°.

2. GOVERNING EQUATIONS

The equations governing the incompressible viscous fluid flow in two dimensions are the equation of continuity and the two components of the momentum equation. In absence of body

forces and heat transfer, these equations can be expressed in the non-dimensional primitive variable form as follows:

Continuity equation:

$$\frac{\partial u}{\partial x}+\frac{\partial v}{\partial y}=0 \tag{1}$$

Momentum equations:
x-momentum:

$$\frac{\partial u}{\partial t}+\frac{\partial (uu)}{\partial x}+\frac{\partial (vu)}{\partial y}=-\frac{\partial p}{\partial x}+\frac{1}{Re}\left(\frac{\partial^2 u}{\partial x^2}+\frac{\partial^2 u}{\partial y^2}\right) \tag{2}$$

y-momentum:

$$\frac{\partial v}{\partial t}+\frac{\partial (uv)}{\partial x}+\frac{\partial (vv)}{\partial y}=-\frac{\partial p}{\partial y}+\frac{1}{Re}\left(\frac{\partial^2 v}{\partial x^2}+\frac{\partial^2 v}{\partial y^2}\right) \tag{3}$$

where the velocity components u and v are along the coordinate directions x and y, respectively, p is ratio of pressure and density, and Re is the Reynolds number.

3. FINITE VOLUME DISCRETIZATION OF GOVERNING EQUATIONS

To obtain a numerical solution, the governing flow equations are discretized by a finite volume technique based on the integral form of the equations to be solved. The physical region, in which the equations are solved, is divided into elementary quadrilateral cells within which the integration is performed. Such a procedure allows one to deal with complicated geometries without considering the equations written in curvilinear coordinates. This also preserves the properties of conservation. Only the coordinates of the corners of the cells are necessary and curvilinear coordinates, not necessarily orthogonal, can be used to define the set of cells. In the present investigation a structured O-grid comprising of quadrilateral cells is generated using Laplace equation.

For an arbitrary quadrilateral cell 'P' as shown in Figure 1, Equations (1)–(3) can be written in integral form as

Continuity equation:

$$\iint_{\Omega}\left(\frac{\partial u}{\partial x}+\frac{\partial v}{\partial y}\right)\mathrm{d}\Omega=0 \tag{4}$$

Momentum equations:
x-momentum:

$$\begin{aligned}&\iint_{\Omega}\left(\frac{\partial u}{\partial t}\right)\mathrm{d}\Omega+\iint_{\Omega}\left(\frac{\partial (uu)}{\partial x}+\frac{\partial (vu)}{\partial y}\right)\mathrm{d}\Omega\\&\quad=-\iint_{\Omega}\left(\frac{\partial p}{\partial x}\right)\mathrm{d}\Omega+\iint_{\Omega}\frac{1}{Re}\times\left[\frac{\partial}{\partial x}\left(\frac{\partial u}{\partial x}\right)+\frac{\partial}{\partial y}\left(\frac{\partial u}{\partial y}\right)\right]\mathrm{d}\Omega\end{aligned} \tag{5}$$

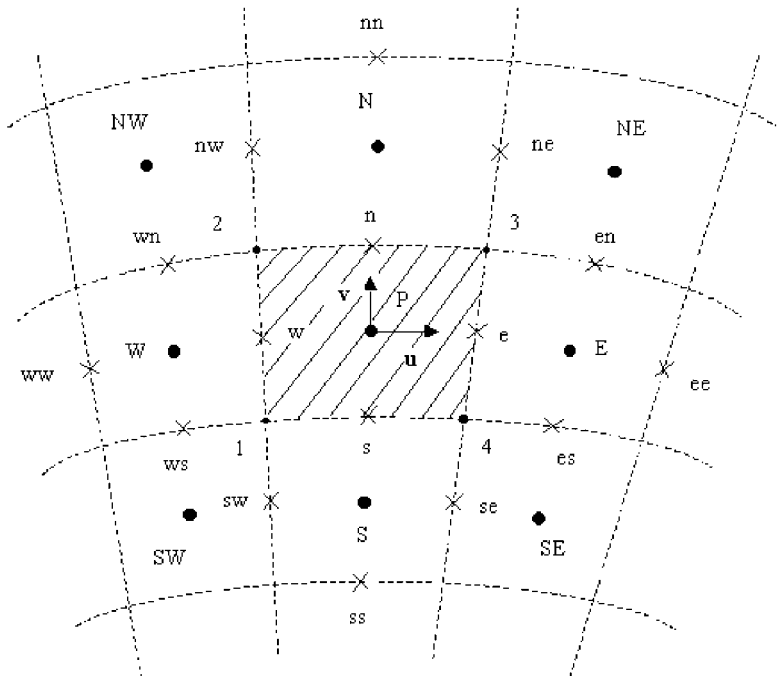

Figure 1. Grid arrangement showing the quadrilateral collocated main control volumes.

y-momentum:

$$\iint_{\Omega}\left(\frac{\partial v}{\partial t}\right)\mathrm{d}\Omega+\iint_{\Omega}\left(\frac{\partial(uv)}{\partial x}+\frac{\partial(vv)}{\partial y}\right)\mathrm{d}\Omega$$
$$=-\iint_{\Omega}\left(\frac{\partial p}{\partial y}\right)\mathrm{d}\Omega+\iint_{\Omega}\frac{1}{Re}\times\left[\frac{\partial}{\partial x}\left(\frac{\partial v}{\partial x}\right)+\frac{\partial}{\partial y}\left(\frac{\partial v}{\partial y}\right)\right]\mathrm{d}\Omega \tag{6}$$

where Ω represents a two-dimensional flow domain. Applying Green's theorem to Equations (4)–(6) for any cell 'P' yields:

Continuity equation:

$$\iint_{\Omega}\left(\frac{\partial u}{\partial x}+\frac{\partial v}{\partial y}\right)\mathrm{d}\Omega=\oint_{C}(u\times\mathrm{d}y-v\times\mathrm{d}x)$$
$$=(u_{\mathrm{e}}\times\Delta y_{43}-v_{\mathrm{e}}\times\Delta x_{43})+(u_{\mathrm{n}}\times\Delta y_{32}-v_{\mathrm{n}}\times\Delta x_{32})$$
$$+(u_{\mathrm{w}}\times\Delta y_{21}-v_{\mathrm{w}}\times\Delta x_{21})+(u_{\mathrm{s}}\times\Delta y_{14}-v_{\mathrm{s}}\times\Delta x_{14})$$
$$+O(|r_{12}|^{3},\ldots)=0 \tag{7}$$

Momentum equations:

unsteady term:

$$\iint_{\Omega}\left(\frac{\partial\phi}{\partial t}\right)\mathrm{d}\Omega=\left(\frac{\partial\phi}{\partial t}\right)\times a_{\mathrm{P}}=\left(\frac{\phi_{\mathrm{P}}^{n+1}-\phi_{\mathrm{P}}^{n}}{\Delta t}\right)\times a_{\mathrm{P}} \tag{8a}$$

convective terms:

$$\begin{aligned}\iint_{\Omega}\left(\frac{\partial(u\phi)}{\partial x}+\frac{\partial(v\phi)}{\partial y}\right)\mathrm{d}\Omega&=\oint_{C}((u\phi)\times\mathrm{d}y-(v\phi)\times\mathrm{d}x)\\&=((u\phi)_{\mathrm{e}}\times\Delta y_{43}-(v\phi)_{\mathrm{e}}\times\Delta x_{43})\\&\quad+((u\phi)_{\mathrm{n}}\times\Delta y_{32}-(v\phi)_{\mathrm{n}}\times\Delta x_{32})+((u\phi)_{\mathrm{w}}\times\Delta y_{21}\\&\quad-(v\phi)_{\mathrm{w}}\times\Delta x_{21})+((u\phi)_{\mathrm{s}}\times\Delta y_{14}\\&\quad-(v\phi)_{\mathrm{s}}\times\Delta x_{14})+O(|r_{12}|^{3},\ldots)\end{aligned} \tag{8b}$$

pressure terms:

$$\begin{aligned}\iint_{\Omega}\left(\frac{\partial p}{\partial x}\right)\mathrm{d}\Omega&=\oint_{C}p\times\mathrm{d}y=p_{\mathrm{e}}\times\Delta y_{43}+p_{\mathrm{n}}\times\Delta y_{32}\\&\quad+p_{\mathrm{w}}\times\Delta y_{21}+p_{\mathrm{s}}\times\Delta y_{14}+O(|r_{12}|^{3},\ldots)\end{aligned} \tag{8c}$$

$$\begin{aligned}\iint_{\Omega}\left(\frac{\partial p}{\partial y}\right)\mathrm{d}\Omega&=-\oint_{C}p\times\mathrm{d}x\\&=-[p_{\mathrm{e}}\Delta x_{43}+p_{\mathrm{n}}\times\Delta x_{32}+p_{\mathrm{w}}\\&\quad\times\Delta x_{21}+p_{\mathrm{s}}\times\Delta x_{14}+O(|r_{12}|^{3},\ldots)]\end{aligned} \tag{8d}$$

diffusive terms:

$$\begin{aligned}&\iint_{\Omega}\frac{1}{Re}\times\left[\frac{\partial}{\partial x}\left(\frac{\partial\phi}{\partial x}\right)+\frac{\partial}{\partial y}\left(\frac{\partial\phi}{\partial y}\right)\right]\mathrm{d}\Omega\\&=\frac{1}{Re}\times\oint_{C}\left[\left(\frac{\partial\phi}{\partial x}\right)\times\mathrm{d}y-\left(\frac{\partial\phi}{\partial y}\right)\times\mathrm{d}x\right]\\&=\frac{1}{Re}\times\left[\left(\frac{\partial\phi}{\partial x}\right)_{\mathrm{e}}\times\Delta y_{43}-\left(\frac{\partial\phi}{\partial y}\right)_{\mathrm{e}}\times\Delta x_{43}+\left(\frac{\partial\phi}{\partial x}\right)_{\mathrm{n}}\times\Delta y_{32}-\left(\frac{\partial\phi}{\partial y}\right)_{\mathrm{n}}\times\Delta x_{32}\right.\\&\quad+\left(\frac{\partial\phi}{\partial x}\right)_{\mathrm{w}}\times\Delta y_{21}-\left(\frac{\partial\phi}{\partial y}\right)_{\mathrm{w}}\times\Delta x_{21}+\left(\frac{\partial\phi}{\partial x}\right)_{\mathrm{s}}\\&\quad\left.\times\Delta y_{14}-\left(\frac{\partial\phi}{\partial y}\right)_{\mathrm{s}}\times\Delta x_{14}+O(|r_{12}|^{3},\ldots\right]\end{aligned} \tag{8e}$$

where u_e, v_e, u_n, v_n, u_w, v_w, u_s and v_s are the cell face centre velocities and p_e, p_n, p_w and p_s are the cell face centre pressures on east, north, west and south faces, respectively, ϕ is the convective flux term and is equal to u and v along x and y directions, respectively, and $(1/Re)\times(\partial\phi/\partial x)$ and $(1/Re)\times(\partial\phi/\partial y)$ are the cell face centre diffusive fluxes. The values of the velocity derivatives are obtained by using Taylor series expansion about the cell face centre points [13]. For example, the velocity derivatives on the east face of the cell 'P' can be expressed as follows:

$$\left(\frac{\partial\phi}{\partial x}\right)_e = \frac{(\phi_E-\phi_P)\times\Delta y_{43}-(\phi_3-\phi_4)\times\Delta y_{PE}}{\Delta x_{PE}\times\Delta y_{43}-\Delta x_{43}\times\Delta y_{PE}} \tag{9a}$$

$$\left(\frac{\partial\phi}{\partial y}\right)_e = -\frac{(\phi_E-\phi_P)\times\Delta x_{43}-(\phi_3-\phi_4)\times\Delta x_{PE}}{\Delta x_{PE}\times\Delta y_{43}-\Delta x_{43}\times\Delta y_{PE}} \tag{9b}$$

Δ is the spacing operator, e.g. $\Delta x_{12}=x_2-x_1$. 'C' is the contour of the cell 'P' and $O(|r_{12}|^3,\ldots)$ is the Newton–Cotes integration error [13].

In Equation (8a), the transient term is approximated using the 'lumped mass' approach, [11, 14]. In this equation the superscript of ϕ stands for the particular time step, namely nth or $(n+1)$th. Δt is the time interval. a_P represents the area of the cell P. The value of the variable at the cell centre, namely u_P, is used as the representative value for the entire cell for evaluating the transient term. The explicit Forward Euler method has been used for discretizing the time derivative that is first-order accurate in time.

4. CONSISTENT FLUX RECONSTRUCTION SCHEME

Based on the above finite volume discretization of the governing equations, an explicit two-dimensional solver has been developed. The solver makes use of collocated grid arrangement where the flow variables u, v and p share the same location at the centre of the cells. For the calculation of convective and pressure fluxes through the cell faces, the unknown values (i.e. u_e, v_e, u_n, v_n, u_w, v_w, u_s, v_s, p_e, p_n, p_w and p_s) at the centre of the cell faces need to be evaluated.

The cell face centre velocities are obtained by using a CFR scheme, which has been developed in the present investigation. The present approach involves the solution of x and y components of the momentum equations at the centre of the cell faces of each cell. This provides the solution for the required cell face centre velocities u_e, v_e, u_n, v_n, u_w, v_w, u_s and v_s for flux calculation. These values are then substituted into the discrete continuity equation to obtain the discrete Poisson equation for pressure. In order to maintain the accuracy of the finite volume discretization, the cell face velocities are approximated by a second-order accurate closure method. The cell face centre pressures are obtained by linearly interpolating the cell centre pressure values calculated by solving the pressure Poisson equation.

When the cell face velocities are obtained by linear interpolation, the cell face velocity, e.g. u_e, on the east face, comes as a function of the cell centre values of the u-velocity component of the concerned cell and its neighbours, but is independent of the corresponding v-velocity component and pressure. Although upwind interpolation schemes can be used to

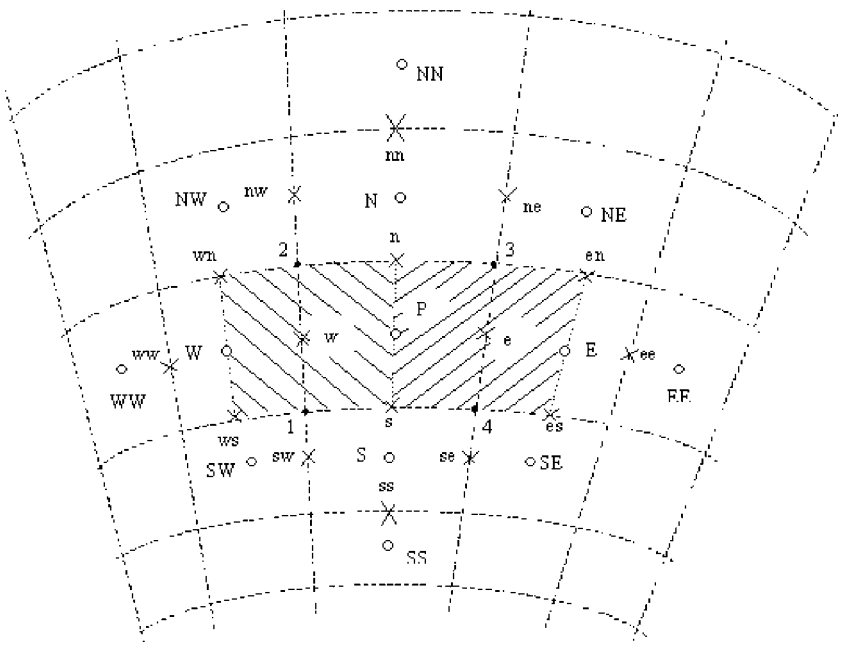

Figure 2. Grid arrangements showing the control volumes for calculation of cell face velocities at the east (e) and west (w) faces.

circumvent the numerical instability problems, spurious pressure modes exist when such linear interpolation formulae are implemented on collocated grids.

One of the most effective means to overcome this difficulty is to use a physically consistent flux reconstruction approach by which the cell face velocities are expressed not only in terms of the dependent variable u, in this case, but also other physical quantities v and p.

In the present solver, a fully explicit scheme is adopted for the reconstruction of cell face velocities as well as for updating the flow variables at the cell centres. A 9-point stencil is used for the pressure equation and a 13-point stencil for the velocity calculations. For calculating the viscous fluxes on the east face of 'e' cell (flux reconstruction cell centred about 'e', Figure 2), for example, the values of velocities at points 'e', 'en', 'ee' and 'es' are necessary. The value of the velocity component at 'ee' is obtained by linear interpolation of the cell centre velocity at E and the cell centre velocity of the cell located on the east of cell 'E', i.e. the cell 'EE' (Figure 2). In this manner the cell 'EE' gets included in the stencil for velocity calculation. In a similar manner, the cells located north of cell 'N' ('NN'), west of cell 'W' ('WW') and south of cell 'S' ('SS') also get included in the stencil. Therefore, the stencil finally includes 13 cells, namely, 'P', 'E', 'NE', 'N', 'NW', 'W', 'SW', 'S', 'SE' and the four additional cells mentioned above, namely, 'EE', 'NN', 'WW' and 'SS'. For updating the flow variables at the cell centres, the momentum equations are solved in an explicit manner in contrast to the implicit scheme of Deng *et al.* [12]. The layout of the flux reconstruction cells used in the present solver is different from that of Deng *et al.* [12]. For example, the 'e' cell includes the points 'E', '3', 'P' and '4' at the cell face centres, which is different from the corresponding cell of Deng *et al.* [12].

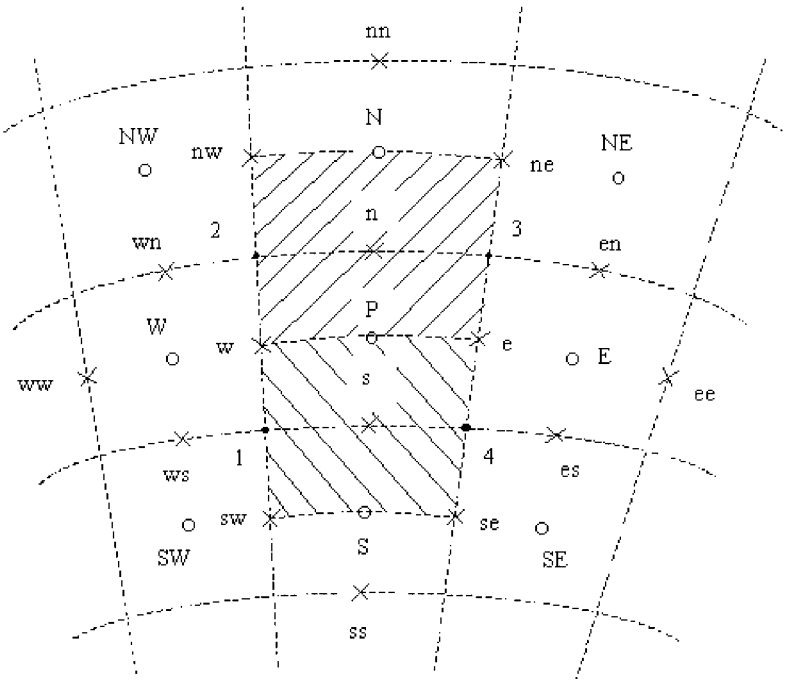

Figure 3. Grid arrangements showing the control volumes for calculation of cell face velocities at the north (n) and south (s) faces.

The closures for the cell face velocities u_e, v_e, u_n, v_n, u_w, v_w, u_s and v_s are derived by writing the discretized u and v components of the momentum equations at the points 'e', 'n', 'w' and 's', respectively (Figures 2 and 3). The finite volume schemes used at these points are similar to that used at point 'P'. The discretization of the various terms are given as follows:

unsteady term:

$$\iint_{\Omega_e} \left(\frac{\partial u}{\partial t}\right)_e \mathrm{d}\Omega_e = \left(\frac{\partial u}{\partial t}\right)_e \times a_e = \left(\frac{u_e^{n+1} - u_e^n}{\Delta t}\right) \times 0.5 \times (a_P + a_E) \tag{10a}$$

convective term:

$$\begin{aligned} \iint_{\Omega_e} \left(\frac{\partial(uu)}{\partial x} + \frac{\partial(vu)}{\partial y}\right)_e \mathrm{d}\Omega_e &= \oint_{C_e} ((uu) \times \mathrm{d}y - (vu) \times \mathrm{d}x) \\ &= u_E^2 \times \Delta y_{es,en} - v_E \times u_E \times \Delta x_{es,en} + u_3^2 \times \Delta y_{en,n} - v_3 \times u_3 \\ &\quad \times \Delta x_{en,n} + u_P^2 \times \Delta y_{n,s} - v_P \times u_P \times \Delta x_{n,s} + u_4^2 \times \Delta y_{s,es} - v_4 \\ &\quad \times u_4 \times \Delta x_{s,es} + O(|r_{12}|^3, \ldots) = \mathrm{UCFLUXe} \end{aligned} \tag{10b}$$

pressure term:

$$\iint_{\Omega_e} \left(\frac{\partial p}{\partial x}\right)_e d\Omega_e = \oint_{C_e} p \times dy$$
$$= p_E \times \Delta y_{es,en} + p_3 \times \Delta y_{en,n} + p_P \times \Delta y_{n,s} + p_4 \times \Delta y_{s,es}$$
$$+ O(|r_{12}|^3, \ldots) = \text{UPFLUXe} \tag{10c}$$

diffusive term:

$$\iint_{\Omega_e} \frac{1}{Re} \times \left[\frac{\partial}{\partial x}\left(\frac{\partial u}{\partial x}\right) + \frac{\partial}{\partial y}\left(\frac{\partial u}{\partial y}\right)\right]_e d\Omega_e$$
$$= \oint_{C_e} \frac{1}{Re} \times \left[\left(\frac{\partial u}{\partial x}\right) \times dy - \left(\frac{\partial u}{\partial y}\right) \times dx\right]$$
$$= \frac{1}{Re} \times \left[\left(\frac{\partial u}{\partial x}\right)_E \times \Delta y_{es,en} - \left(\frac{\partial u}{\partial y}\right)_E \times \Delta x_{es,en} + \left(\frac{\partial u}{\partial x}\right)_3 \times \Delta y_{en,n} - \left(\frac{\partial u}{\partial y}\right)_3 \times \Delta x_{en,n}\right.$$
$$+ \left(\frac{\partial u}{\partial x}\right)_P \times \Delta y_{n,s} - \left(\frac{\partial u}{\partial y}\right)_P \times \Delta x_{n,s} + \left(\frac{\partial u}{\partial x}\right)_4 \times \Delta y_{s,es} - \left(\frac{\partial u}{\partial y}\right)_4 \times \Delta x_{s,es}$$
$$\left. + O(|r_{12}|^3, \ldots)\right] = \text{UDFLUXe} \tag{10d}$$

In Equation (10a), the 'lumped mass' approach has been applied to the flux reconstruction cell on the east face of the cell P. The area of the reconstruction cell is half the sum of the areas of cells P and E. The value of the variable at the reconstruction cell centre, namely u_e, is used as the representative value for the entire reconstruction cell for evaluating the transient term. Ω_e is the domain of the 'e' cell and C_e is the contour enclosing it. The values of properties at the various nodal points like 1, 2, 3, 4, etc., are obtained by linear interpolation of neighbouring cell centre property values. For example, the equation used for evaluating the value of the property at point 1 is given as follows:

$$\phi_1 = \frac{(a_W + a_P)^2 \times (a_{SW}\phi_S + a_S\phi_{SW}) + (a_{SW} + a_S)^2 \times (a_W\phi_P + a_P\phi_W)}{(a_{SW} + a_S) \times (a_W + a_P) \times (a_W + a_P + a_S + a_{SW})} \tag{11}$$

The above expression is obtained by first calculating the values of the property at 'w' and 'sw' points by linear interpolation from neighbouring cell centre values and then again linearly interpolating these values to obtain the value of the property at point '1'. The first-order velocity derivatives $(\partial\phi/\partial x)$ and $(\partial\phi/\partial y)$ at points E, 3, P and 4 are obtained using Taylor series expansion. For example, the velocity derivatives at point 'E' are given as follows:

$$\left(\frac{\partial\phi}{\partial x}\right)_E = \frac{(\phi_{ee} - \phi_e) \times \Delta y_{es,en} - (\phi_{en} - \phi_{es}) \times \Delta y_{e,ee}}{\Delta x_{e,ee} \times \Delta y_{es,en} - \Delta x_{es,en} \times \Delta y_{e,ee}} \tag{12a}$$

$$\left(\frac{\partial\phi}{\partial y}\right)_E = -\frac{(\phi_{ee} - \phi_e) \times \Delta x_{es,en} - (\phi_{en} - \phi_{es}) \times \Delta x_{e,ee}}{\Delta x_{e,ee} \times \Delta y_{es,en} - \Delta x_{es,en} \times \Delta y_{e,ee}} \tag{12b}$$

The velocity derivatives at the other integration points and on other faces (n, w and s) are calculated using similar formulae. The closure interpolation formula for u_e can be derived from the substitution of Equations (10a)–(10d) into Equation (5). The resulting expression for u_e at the $(n+1)$th time level is

$$u_e^{n+1} = u_e^n + \frac{1}{0.5 \times (a_P + a_E)} \times (-\text{UCFLUXe} - \text{UPFLUXe} + \text{UDFLUXe}) \times \Delta t \tag{13}$$

The cell face velocity at nth time level i.e. u_e^n is taken as the linear interpolation of the adjoining nodal values at that time level. In a similar manner Equations (5) and (6) are solved to obtain the flux closure relationships for v_e, u_n, v_n, u_w, v_w, u_s and v_s, respectively, at the $(n+1)$th time level.

At the body boundary cells no velocity reconstruction is necessary on the south face because no-slip velocity boundary condition is applied. For reconstruction on the east and west cell faces, the calculations are done with due care by enforcing no slip at all the nodal points which lie on the body boundary, namely, 'ws', '1', 's', '4' and 'es'. The value of pressure at all the body boundary points are obtained from the neighbouring flow field points by applying the zero normal pressure gradient condition. The velocity derivatives on the body boundary are calculated by assuming a layer of ghost cells below the body (reflection principle), where the properties at each node of a ghost cell are equal in magnitude but opposite in sign to the corresponding nodal value of the body boundary cell. At the outer boundary, solution of the discretized flux reconstruction equations are obtained up to the $(N-1)$th cells. At the north face of these $(N-1)$th cells, flux reconstruction is performed on the basis of the last time step values available at the cell centres of the Nth cells, if it is the outlet boundary, or on the basis of the free stream values if it is the inlet boundary. A similar approach as explained above is followed for solving the momentum and pressure equations at the body boundary and outer boundary.

5. THE PRESSURE POISSON EQUATION

The equation for pressure is derived by substituting the expressions for u_e^{n+1}, v_e^{n+1}, u_n^{n+1}, v_n^{n+1}, u_w^{n+1}, v_w^{n+1}, u_s^{n+1} and v_s^{n+1} into the discrete continuity equation (Equation (7)). The following pressure Poisson equation is obtained with pressure as unknown:

$$\begin{aligned} p_P = \frac{1}{C_P} \times [&\text{SOURCE} - C_E \times p_E - C_N \times p_N - C_W \times p_W - C_S \times p_S \\ &- C_{NE} \times p_{NE} - C_{SE} \times p_{SE} - C_{NW} \times p_{NW} - C_{SW} \times p_{SW}] \end{aligned} \tag{14}$$

where the coefficients C_E, C_N, C_W, C_S, C_{NE}, C_{SE}, C_{NW} and C_{SW} are the geometrical parameters of the cell and SOURCE is the total source term comprising of the cell divergence at the nth time level, $D_{i,j}^n$, and the convective and diffusive fluxes at the cell faces. The term SOURCE is an explicit function of the nodal variables $u_{i,j}$ and $v_{i,j}$ which include the concerned cell and its eight neighbours as given below.

$$\begin{aligned} \text{SOURCE} = (&u_e \times \Delta y_{43} + u_n \times \Delta y_{32} + u_w \times \Delta y_{21} + u_s \times \Delta y_{14} \\ &- v_e \times \Delta x_{43} - v_n \times \Delta x_{32} - v_w \times \Delta x_{21} - v_s \times \Delta x_{14})^n / \Delta t \end{aligned}$$

$$
\begin{aligned}
&+\left(\mathrm{UCFLUXe}+\frac{1}{Re}\times\mathrm{UDFLUXe}\right)\times\frac{\Delta y_{43}}{a_{\mathrm{e}}}\\
&+\left(\mathrm{UCFLUXn}+\frac{1}{Re}\times\mathrm{UDFLUXn}\right)\times\frac{\Delta y_{32}}{a_{\mathrm{n}}}\\
&+\left(\mathrm{UCFLUXw}+\frac{1}{Re}\times\mathrm{UDFLUXw}\right)\times\frac{\Delta y_{21}}{a_{\mathrm{w}}}\\
&+\left(\mathrm{UCFLUXs}+\frac{1}{Re}\times\mathrm{UDFLUXs}\right)\times\frac{\Delta y_{14}}{a_{\mathrm{s}}}\\
&-\left(\mathrm{VCFLUXe}+\frac{1}{Re}\times\mathrm{VDFLUXe}\right)\times\frac{\Delta x_{43}}{a_{\mathrm{e}}}\\
&-\left(\mathrm{VCFLUXn}+\frac{1}{Re}\times\mathrm{VDFLUXn}\right)\times\frac{\Delta x_{32}}{a_{\mathrm{n}}}\\
&-\left(\mathrm{VCFLUXw}+\frac{1}{Re}\times\mathrm{VDFLUXw}\right)\times\frac{\Delta x_{21}}{a_{\mathrm{w}}}\\
&-\left(\mathrm{VCFLUXs}+\frac{1}{Re}\times\mathrm{VDFLUXs}\right)\times\frac{\Delta x_{14}}{a_{\mathrm{s}}} \qquad (15)
\end{aligned}
$$

where expressions for UCFLUXe and UDFLUXe are provided in Equations (10b) and (10d), respectively. The expressions for the remaining flux terms are similarly obtained from the other cell face centres.

Equation (14) is used directly as the pressure equation in a decoupled approach to determine the pressure field in various cells. It involves nine neighbouring nodes NE, E, SE, N, P, S, NW, W and SW. In case of Cartesian coordinates, the Pressure equation involves only five nodes E, N, W, S and P.

For the cells near the body boundary, the expression for the pressure equation is obtained by applying the zero velocity boundary condition in the discretized continuity equation. Zero normal pressure gradient across the body boundary is applied in Equation (14). Pressure on the body boundary is obtained by using the Neumann boundary condition and special care is taken to satisfy the compatibility condition [15, 16] in the discretized pressure Poisson equation for such cells. Satisfaction of the compatibility condition ensures that there is zero net source term when the discretized equations over the entire computational domain are considered.

Dirichlet boundary condition of free-stream pressure has been applied in the inlet portion of the outer boundary of the domain. At the outlet portion of the outer boundary, the traction-free condition proposed by Gresho [17] has been applied, which provides the following condition for the dimensional pressure:

$$p_{\mathrm{outlet}} = 2\mu\left(\frac{\partial u_{\mathrm{n}}}{\partial n}\right) \qquad (16)$$

where 'n' is the local normal direction to the boundary and 'u_{n}' is the normal component of the total velocity at the outlet boundary. This boundary condition allows for the pressure

wave propagation. It is interesting to note that for simulation of two-dimensional unconfined flow past square and rectangular cylinder, Tamura and Kuwahara [18] and Tamura *et al.* [19] have used the Dirichlet boundary condition of free-stream pressure at the outer boundary of the domain.

The iterative method using successive over-relaxation has been used to solve the pressure Poisson equation [20]. In the present computation a value of 1.5 has been used as the over-relaxation factor. Once the pressure Poisson equation is solved, the cell centre pressure values are available. The cell face centre pressures are obtained by linear interpolation of adjacent cell centre values. For example, the east cell face centre pressure is obtained as

$$p_e = \frac{p_E \times a_P + p_P \times a_E}{a_P + a_E} \tag{17}$$

6. RECONSTRUCTION OF CELL CENTRE MOMENTUM EQUATIONS

The reconstructed cell centre momentum equations are obtained by substituting the values of velocity derivatives at cell face centres, interpolated cell face centre pressures, and the values of the cell face centre velocities obtained by the CFR approach formulated in the present investigation into the discretized momentum equations. From these equations, the velocities at the cell centres are calculated and updated in time explicitly.

7. INITIAL CONDITION

The governing equations for viscous incompressible flow are mixed parabolic–elliptic in nature. The equations are parabolic with respect to time and elliptic with respect to space. This means that the solution marches forward in time due to the parabolic behaviour and disturbances may travel along any direction, upstream or downstream due to the elliptic behaviour. Therefore, initial conditions need to be set at the beginning of the solution and boundary conditions surrounding the domain should be specified.

In the beginning of the solution process, uniform free-stream velocity and pressure field are prescribed in each cell of the flow domain as given below.

$$\left.\begin{aligned} u(i,j) = u_\infty = U_\infty \times \cos\alpha \\ v(i,j) = v_\infty = U_\infty \times \sin\alpha \\ p(i,j) = p_\infty \end{aligned}\right\} \quad \text{for all } 1 \leqslant i \leqslant M,\ 1 \leqslant j \leqslant N \tag{18}$$

This physically means that the body is suddenly introduced into a uniform free-stream flow. The flow domain has been discretized using $M \times N$ cells (M cells along ξ_g and N cells along η_g, where ξ_g and η_g are the grid-aligned coordinates in the circumferential and radial directions). Angle of incidence is given by α. Free stream flow parameters are indicated by suffix ∞.

8. BOUNDARY CONDITIONS

For the O-grid system, only two boundaries exist: inlet (upstream) and outlet (downstream). Both the inlet and the outlet boundaries are kept far away from the body surface, at a distance

of 26*B*. At the inlet, the streamwise velocity component is assigned as that of the free stream and at the outlet boundary, both transverse and the streamwise components are obtained by applying the continuity boundary condition. On the body surface, no-slip condition is applied.

Numerical simulations of Sohankar *et al.* [21] reveal that when solving unconfined flow past a body, if the outer boundary of the computational domain is placed at a minimum distance of 26 times the chord of the body, it has no profound effect on the flow field in the immediate vicinity of the body. The far field is located a long distance away to minimize the chances of waves reflecting back from the outlet boundary and to ensure minimum distortion of the velocity field as it leaves the boundary. Non-reflecting or open boundary conditions can reduce such reflections, though implementing them in the numerical scheme would be more involved. The pioneering work in that direction has been reported by Orlanski [22]. Some other researchers who have developed such open boundary conditions in the recent times are Bruneau and Fabrie [23] and Hasan *et al.* [24]. Sohankar *et al.* [21] have investigated the effects of various outlet boundary conditions on the solution while solving unconfined flow past a square cylinder.

9. NUMERICAL STABILITY CRITERIA

The stability of an explicit numerical scheme is mainly dependent on the time step employed in the calculation procedure. Because of the explicit scheme, this time step is highly restricted to obtain a stable and accurate solution. In the present computation, this time step is obtained by taking the contribution of the inviscid and viscous fluxes separately. The contribution of the inviscid fluxes to the time step is usually restricted by the local CFL criterion which allows the fluid to traverse only one cell at one time step. To account for the viscous effects, this time step has been suitably modified. However, rigorous stability analysis of the discretized equations on curvilinear coordinates has not been performed to find out the exact contributions.

Let V_{ξ_g} and V_{η_g} be the components of the velocity vector along the two grid-aligned directions. These velocity components are obtained by taking a dot product of the cell centre velocity vector and unit vectors along ξ_g and η_g directions. Then by CFL criteria

$$\delta t < \min\left\{\frac{\Delta\xi_g}{|V_{\xi_g}|}, \frac{\Delta\eta_g}{|V_{\eta_g}|}\right\} \tag{19a}$$

where $\Delta\xi_g$ and $\Delta\eta_g$ are the extents of a cell along ξ_g and η_g directions, respectively. Sotiropoulos and Abdallah [4], Hwang and Sue [25] and several other researchers have used such CFL-number-based time step calculation in various incompressible Navier–Stokes solvers. The minimum time step by considering the viscous effects is calculated as follows:

$$\delta t = \frac{0.5 \times Re}{\left\{\dfrac{1}{(\Delta\xi_g)^2} + \dfrac{1}{(\Delta\eta_g)^2}\right\}} \tag{19b}$$

The lowest δt as evaluated from Equations (19a) and (19b) is obtained for all cells of the field. For the computational purposes, only a fraction of the smallest time step of all the grid cells is considered to ensure stability of the solution.

10. SUMMARY OF STEPS IN A CALCULATION CYCLE

The various steps involved in the present computation can be summarized as follows:

(1) The velocity and the pressure field u^n, v^n and p^n are initialized. This is done either from the result of previous cycle or from the prescribed initial conditions.
(2) The cell face velocities u_e^{n+1}, v_e^{n+1}, u_n^{n+1}, v_n^{n+1}, u_w^{n+1}, v_w^{n+1}, u_s^{n+1} and v_s^{n+1} at $(n+1)$th time level are obtained by solving the x- and y-components of the momentum equations at the centre of the cell faces in terms of nth time level cell-centred velocity and pressure fields u^n, v^n and p^n using the proposed CFR scheme.
(3) The discrete pressure Poisson equation is obtained by substituting the expressions of reconstructed cell face centre velocities in the discrete continuity equation. The discrete pressure Poisson equation is then solved to obtain the pressure field p^{n+1} using the velocity field u^n, v^n of nth time level.
(4) The discrete cell centre momentum equations are then solved to update the cell centre velocity components u^{n+1}, v^{n+1} at the new time level $(n+1)$ in an explicit manner using the reconstructed cell face centre velocities and the pressure p^{n+1} obtained from the pressure equation.

This completes the necessary calculations for advancing the flow field through one cycle in time. The process is repeated until steady state convergence or steady state oscillation is achieved.

A computer code has been developed to solve unconfined flow past a two-dimensional body of arbitrary geometry at angle of incidence. The numerical simulations were performed on a HP9000, 512 MB RAM, 8 GB HDD, OASIS HP-UX, 400 MHz Dual Processor Server. For flow past square cylinder at $Re = 200$, at $\alpha = 0^\circ$ with 160×120 grid, one time step calculation after stabilization of periodicity is 40 s. On increase of the angle of incidence the computing time increases to a peak value of 65 s at $\alpha = 30^\circ$. At $\alpha = 45^\circ$ it decreases to 53 s.

11. RESULTS AND DISCUSSION

In the present investigation initially flow past square cylinder at $Re = 40$, 100, 200 and 500 for $\alpha = 0^\circ$ has been computed. Subsequently, flow past square cylinder at $Re = 100$ and 200 for $\alpha = 5^\circ$–45° has been computed. The overall characteristics like the lift and drag coefficients (C_L and C_D) and Strouhal number (St) are used for the validation of the code. The overall lift and drag coefficients are obtained from the contributions of body surface pressure and shear stress. These overall forces acting on the body can be split into two components: normal force component (F_n) and axial force component (F_a). These individual components can be obtained, by taking the contribution of pressure and viscous effects as shown by Braza *et al.* [26].

The projected width of the body facing the flow can be given as

$$w = B \times (\sin\alpha + \cos\alpha) \tag{20}$$

The lift and the drag coefficients are then calculated based on the projected width of the body in order to compare the computed values of the force coefficients with those of

Table I. Grid independence test.

Grid size	Strouhal number	Average drag coefficient
200×160 (Grid 1)	0.127	1.56
160×120 (Grid 2)	0.1243	1.533
100×80 (Grid 3)	0.11	1.467

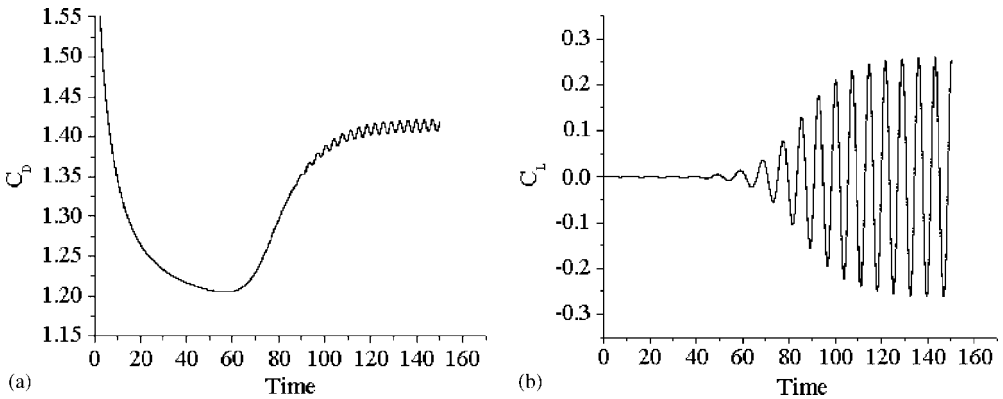

Figure 4. (a) The drag coefficient characteristics for the square cylinder at $Re = 100$ and $\alpha = 0^\circ$; and (b) the lift coefficient characteristics for the square cylinder at $Re = 100$ and $\alpha = 0^\circ$.

Sohankar *et al.* [21], where the above procedure has been adopted.

$$L = F_n \times \cos\alpha - F_a \times \sin\alpha \tag{21a}$$

$$D = F_n \times \sin\alpha + F_a \times \cos\alpha \tag{21b}$$

$$C_L = \frac{L}{0.5\rho_\infty \times (u_\infty^2 + v_\infty^2) \times w} = \frac{L}{0.5\rho_\infty \times (u_\infty^2 + v_\infty^2) \times B \times (\sin\alpha + \cos\alpha)} \tag{21c}$$

$$C_D = \frac{D}{0.5\rho_\infty \times (u_\infty^2 + v_\infty^2) \times w} = \frac{D}{0.5\rho_\infty \times (u_\infty^2 + v_\infty^2) \times B \times (\sin\alpha + \cos\alpha)} \tag{21d}$$

The present computations have been carried out using a 160×120 O-grid. The size of the grid was decided based on a grid independence study carried out on three different grids, namely, 200×160 (grid 1), 160×120 (grid 2) and 100×80 (grid 3) for flow past square cylinder at $Re = 200$ and $\alpha = 0^\circ$. It was found that the maximum difference between the drag coefficient and Strouhal number calculated using grid 1 and grid 2 is of the order of 2%, whereas that between grid 2 and grid 3 is 4%. Therefore, grid 2 has been chosen for the flow calculations. Table I gives the details of the grid independence test.

The time-dependent drag and lift coefficient characteristics for the square cylinder at $Re = 100$ and $\alpha = 0^\circ$ are shown in Figures 4(a) and (b), respectively. After initial fluctuations, the characteristics attain a steady state oscillation after a large value of non-dimensional

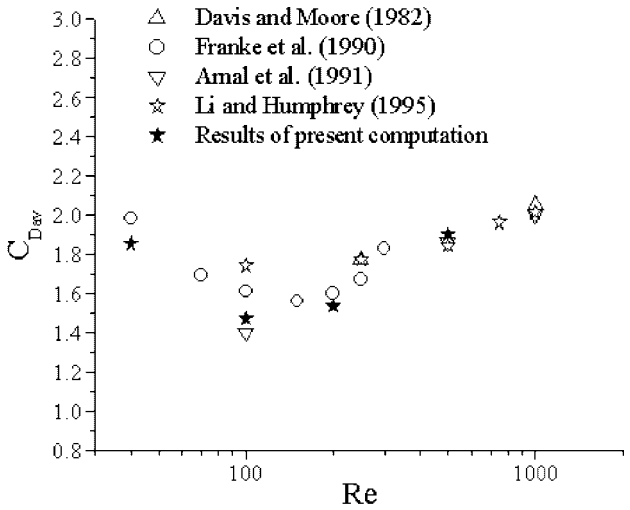

Figure 5. Variation of time-averaged drag coefficient as a function of Reynolds number for flow past square cylinder at $\alpha = 0°$.

time t, typically, $t > 140$, implying unsteady flow. The non-dimensional time 't' is obtained by dividing the dimensional time by a factor (B/U_∞).

The average value of C_D ($C_{D_{av}}$) obtained from the present solver and the results of Davis and Moore [27], Franke *et al.* [28], Arnal *et al.* [29] and Li and Humphrey [30] as a function of Re are shown in Figure 5. The results of the present solver compares well with the results available from literature.

Figure 6 shows the time development of separated flow past square cylinder at $\alpha = 45°$, $Re = 100$. At all the time levels the flow separates from the upper corner of the front face and lower corner of the rear face of the cylinder as seen from the streamlines shown in Figures 6(a)–(d). In the wake of the cylinder, the flow characteristics change significantly with change in time. At $t = 10.01$, a small, symmetric wake is formed behind the cylinder indicating a steady flow behind it. With increase in time the wake grows in length as seen at $t = 25.02$. Subsequently, the symmetric nature of the wake gets gradually distorted and an asymmetry sets in as seen at $t = 40.01$. This phenomenon becomes more significant at higher time levels, and finally the alternate vortex shedding phenomenon sets in as seen at $t = 60.05$ leading to the formation of von Karman vortex street.

Figure 7 shows the vorticity and pressure contours for $\alpha = 45°$, $Re = 100$, $t = 93.0$. The shed vortices follow the path of the free stream. The pressure plots indicate the presence of low-pressure zones behind the cylinder.

The time-dependent surface pressure distribution on the square cylinder for $\alpha = 10°$ at $Re = 100$ is shown in Figure 8. The pressure coefficient at the front-stagnation point is nearly 1.0, which is as expected. Due to the non-zero α, the stagnation point shifts towards $S/B = 1.0$, which is the lower corner of the front face of the cylinder. S/B is the non-dimensional distance along the body surface measured in the anticlockwise direction by starting from the top corner of the front face. It has been observed that unsteadiness in the body surface pressure increases

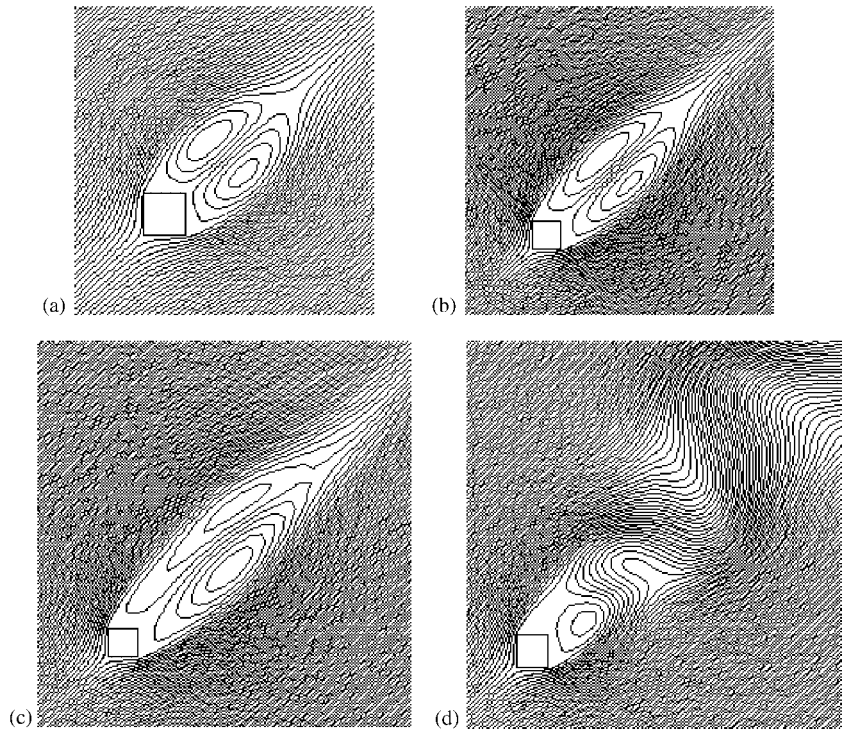

Figure 6. Time development of separated flow past square cylinder at $\alpha = 45^\circ$, $Re = 100$: (a) $t = 10.01$; (b) $t = 25.02$; (c) $t = 40.01$; and (d) $t = 60.05$.

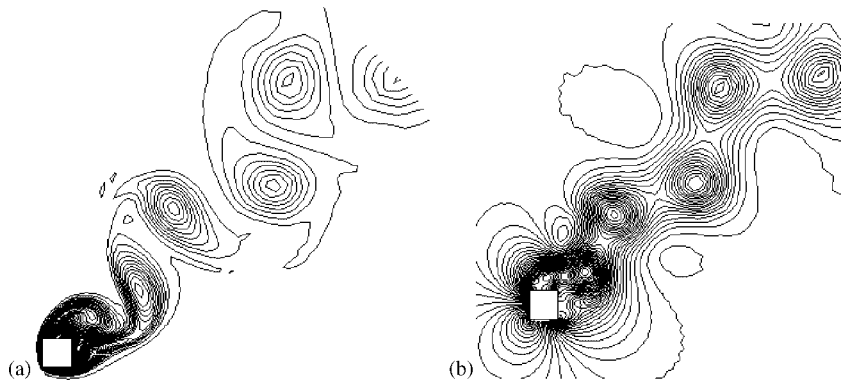

Figure 7. Vorticity contours and pressure contours for $\alpha = 45^\circ$, $Re = 100$, $t = 93.0$.

with increase in α. At the front corners where the flow separates, the body surface pressure (C_P) drops significantly to a negative value and remains negative throughout the separated region.

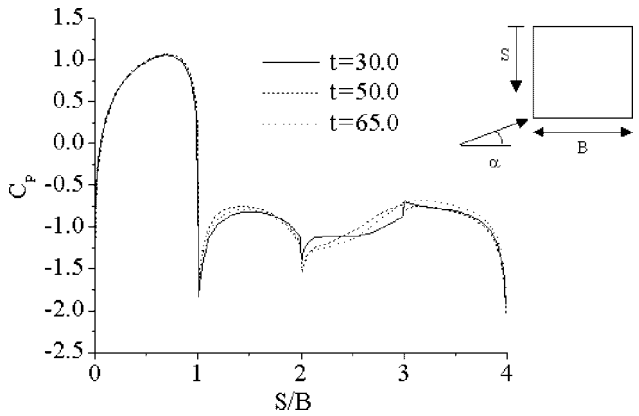

Figure 8. The time variation of surface pressure distribution for $\alpha = 10°$, $Re = 100$.

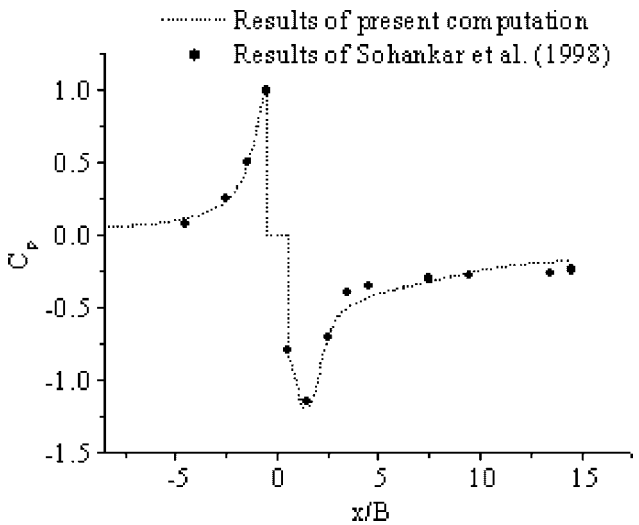

Figure 9. Comparison of time-averaged pressure coefficient along the flow direction between the present solver and results of Sohankar *et al.* [21] for $\alpha = 0°$, $Re = 200$.

Comparison of the time-averaged coefficient of pressure along the flow direction between the present solver and results of Sohankar *et al.* [21] for $Re = 200$ is shown in Figure 9. Reasonably good agreement has been obtained. The pressure in the region ahead of the cylinder is steady and gradually increases to a value of 1.0 at the front stagnation region. The maximum negative pressure in the wake region is formed just behind the cylinder. At large distances downstream, the pressure seems to be recovering gradually to free-stream pressure. It is to be noted that the origin of the coordinate system is fixed at the centre of the square cylinder. The length of a side of square cylinder, B, is taken as unity. Therefore, the rear face of the cylinder corresponds to $x = 0.5$.

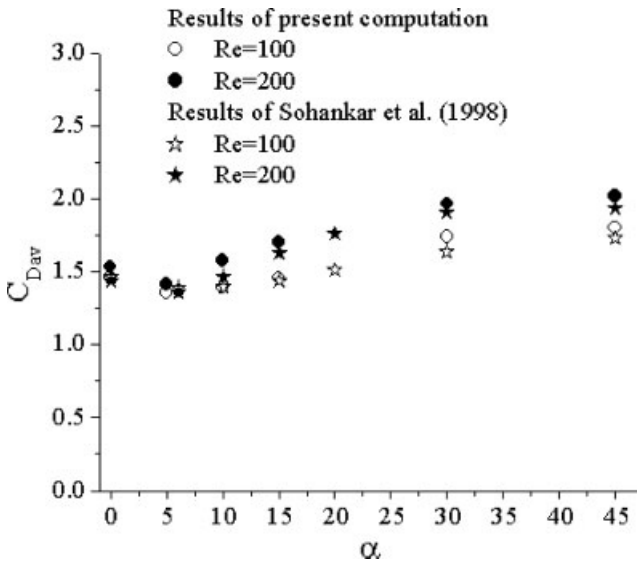

Figure 10. Variation of time-averaged drag coefficient as a function of angle of incidence.

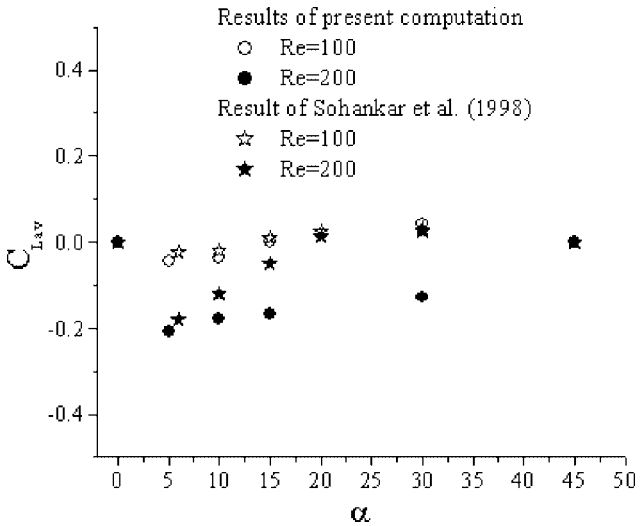

Figure 11. Variation of time-averaged lift coefficient as a function of angle of incidence.

Figure 10 shows the variation of time-averaged drag coefficient as a function of angle of incidence for $Re = 100$ and $Re = 200$. It is observed that the average drag decreases from $\alpha = 0$ to 5°. Subsequently, the average drag coefficient increases monotonically up to $\alpha = 45°$. Fairly close agreement has been obtained with the results of Sohankar *et al.* [21] for both the Reynolds numbers. Figure 11 shows the variation of time-averaged lift coefficient as a

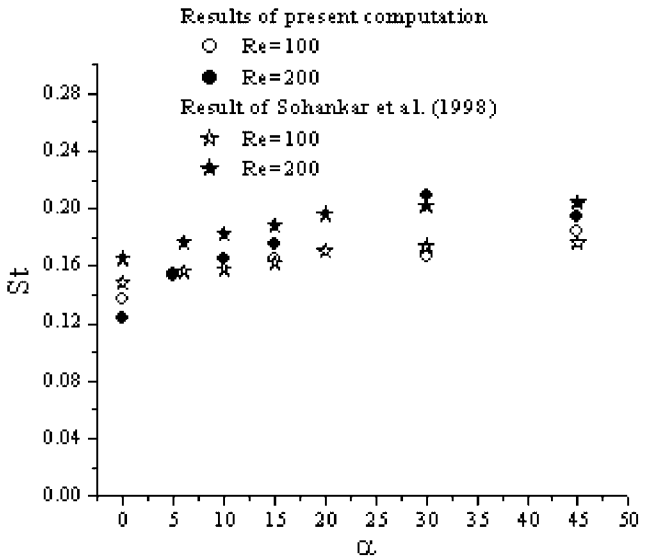

Figure 12. Variation of Strouhal number as a function of angle of incidence.

function of angle of incidence. The lift coefficient is close to zero at $Re = 100$ over the entire range of angles of incidence. A decrease in average lift coefficient is observed for $Re = 200$ from $\alpha = 0$ to 5° with a subsequent increase. Fairly close agreement is obtained with the results of Sohankar *et al.* [21] for $Re = 100$. For most of the test cases for varying angle of incidence and Reynolds number the lift due to pressure was negative (acting downwards) while the lift due to friction was positive (acting upwards) over the square cylinder. At the lower Reynolds number of 100 the frictional lift was greater than the pressure lift, whereas the pressure lift increased with Reynolds number and at a higher Reynolds number of 200 the effect of the pressure lift dominated a wide range of angles of incidence. The present scheme has predicted higher values of pressure lift than frictional lift as compared to Sohankar *et al.* [21] at $Re = 200$, which may be the reason for this discrepancy. Figure 12 shows the variation of Strouhal number as a function of angle of incidence. A gradual increase of Strouhal number with increase in angle of incidence is observed. Also, the Strouhal number at a particular angle of incidence is higher for higher Reynolds number. Fairly good conformity is obtained with the results of Sohankar *et al.* [21] for both the Reynolds numbers.

12. CONCLUSIONS

In the present investigation an explicit two-dimensional incompressible finite volume collocated grid-based Navier–Stokes solver has been developed based on a newly proposed 'consistent flux reconstruction' scheme. The solver is capable of solving unconfined flow past any arbitrary two-dimensional body geometry. A structured curvilinear body-fitted O-grid has been used in the solver, which has been obtained using Laplace equation. In the newly proposed flux reconstruction scheme cell face centre velocities are calculated by solving the momentum

equations at each cell face. The scheme is found to produce reasonably satisfactory results for unconfined flow past square cylinder at zero and non-zero angles of incidence over a range of low and moderate Reynolds numbers when compared with results available from literature. The method can be easily extended to three-dimensional flows.

REFERENCES

1. Harlow FH, Welch JE. Numerical calculation of time-dependent viscous incompressible flow of fluid with free surface. *Physics of Fluids* 1965; **8**(12):2182–2189.
2. Amsden AA, Harlow FH. The SMAC method: a numerical technique for calculating incompressible fluid flows. *Report LA-4370*, Los Alamos Scientific Laboratory, 1970.
3. Hirt CW, Nichols BD, Romero NC. SOLA—a numerical solution algorithm for transient fluid flows. *Report LA-5852*, Los Alamos Scientific Laboratory, 1975.
4. Sotiropoulos F, Abdallah S. Coupled fully implicit solution procedure for the steady incompressible Navier–Stokes equations. *Journal of Computational Physics* 1990; **87**:328–348.
5. Ferjiger JH, Peric M. *Computational Methods for Fluid Dynamics.* Springer: Berlin, 1999.
6. de Foy B, Dawes W. Unstructured pressure-correction solver based on a consistent discretisation of the Poisson equation. *International Journal for Numerical Methods in Fluids* 2000; **34**:463–478.
7. Kim J, Moin P. Application of a fractional-step method to incompressible Navier–Stokes equations. *Journal of Computational Physics* 1985; **59**:308–323.
8. Fletcher CAJ. *Computational Techniques for Fluid Dynamics 2*, *Specific Techniques for Different Flow Categories*. Springer: Berlin, 1988.
9. Melaaen MC. Calculation of fluid flows with staggered and nonstaggered curvilinear non orthogonal grids—the theory. *Numerical Heat Transfer* (*Part B*) 1992; **21**:1–19.
10. Rhie CM, Chow WL. Numerical study of the turbulent flow past an airfoil with trailing edge separation. *AIAA Journal* 1983; **21**(11):1525–1532.
11. Schneider GE, Raw MJ. Control volume finite element method for heat transfer and fluid flow using collocated variables, 1. Computational procedure; 2. Application and validation. *Numerical Heat Transfer* 1987; **11**: 363–400.
12. Deng GB, Piquet J, Queutey P, Visonneau M. Incompressible flow calculations with a consistent physical interpolation finite volume approach. *Computers and Fluids* 1994; **23**(8):1029–1047.
13. Jeng YN, Chen JL. Geometric conservation law of the finite-volume method for the SIMPLER algorithm and a proposed upwind scheme. *Numerical Heat Transfer* (*Part B*) 1992; **22**:211–234.
14. Mukhopadhyay A, Sundararajan T, Biswas G. An explicit transient algorithm for predicting incompressible viscous flows in arbitrary geometry. *International Journal for Numerical Methods in Fluids* 1993; **17**: 975–993.
15. Abdallah S. Numerical solution for the pressure Poisson equation with Neumann boundary condition using a non staggered grid, I. *Journal of Computational Physics* 1987; **70**:182–192.
16. Abdallah S. Numerical solutions for the incompressible Navier–Stokes equation in primitive variables using a non staggered grid, II. *Journal of Computational Physics* 1987; **70**:193–202.
17. Gresho PM. Some current CFD issues relevant to the incompressible Navier–Stokes equations. *Computer Methods in Applied Mechanics and Engineering* 1991; **87**:201–252.
18. Tamura T, Kuwahara K. Numerical study of aerodynamic behaviour of a square cylinder. *Journal of Wind Engineering and Industrial Aerodynamics* 1990; **33**:161–170.
19. Tamura T, Ohta I, Kuwahara K. On the reliability of two-dimensional simulation for unsteady flows around a cylinder-type structure. *Journal of Wind Engineering and Industrial Aerodynamics* 1990; **35**:275–298.
20. Young D. Iterative methods for solving partial differential equations of Elliptic type. *Transactions of the American Mathematical Society* 1954; **76**:92–111.
21. Sohankar A, Norberg C, Davidson L. Low Reynolds-number flow around a square cylinder at incidence: study of blockage, onset of vortex shedding and outlet boundary condition. *International Journal for Numerical Methods in Fluids* 1998; **26**:39–56.
22. Orlanski I. A simple boundary condition for unbounded hyperbolic flows. *Journal of Computational Physics* 1976; **21**:251–269.
23. Bruneau CHH, Fabrie P. Effective downstream boundary conditions for incompressible Navier–Stokes equations. *International Journal for Numerical Methods in Fluids* 1994; **19**:693–705.
24. Hasan N, Anwer SF, Sanghi S. On the outflow boundary condition for external incompressible flows: a new approach. *Journal of Computational Physics* 2005; **206**:661–683.
25. Hwang RR, Sue YC. Numerical simulation of shear effect on vortex shedding behind a square cylinder. *International Journal for Numerical Methods in Fluids* 1997; **25**:1409–1420.

26. Braza M, Chassaing P, Ha Minh H. Numerical study and physical analysis of the pressure and velocity fields in the near wake of a circular cylinder. *Journal of Fluid Mechanics* 1986; **163**:79–130.
27. Davis RW, Moore EF. A numerical study of vortex shedding from rectangles. *Journal of Fluid Mechanics* 1982; **116**:475–506.
28. Franke R, Rodi W, Schonung B. Numerical calculation of laminar vortex shedding flow past cylinders. *Journal of Wind Engineering and Industrial Aerodynamics* 1990; **35**:237–257.
29. Arnal MP, Goering DJ, Humphrey JAC. Vortex shedding from a bluff body on a sliding wall. *Journal of Fluids Engineering* (ASME) 1991; **113**:384–398.
30. Li G, Humphrey JAC. Numerical modelling of confined flow past a cylinder of square cross section at various orientations. *International Journal for Numerical Methods in Fluids* 1995; **20**:1225–1236.

